

**Boolean reconstructions of complex materials: Integral geometric approach**

C. H. Arns\*

*School of Petroleum Engineering, University of New South Wales, Sydney, New South Wales 2052, Australia*

M. A. Knackstedt†

*Department of Applied Mathematics, Research School of Physical Sciences and Engineering,  
Australian National University, Canberra, Australian Capital Territory 0200, Australia*

K. R. Mecke‡

*Institut für Theoretische Physik, Universität Erlangen–Nürnberg, Staudtstraße 7, 91058 Erlangen, Germany*

(Received 18 May 2009; published 30 November 2009)

We show that for the Boolean model of random composite media one can, from a single image of a system at any particle fraction, define a set of parameters which allows one to accurately reconstruct the medium for all other phase fractions. The morphological characterization is based on a family of measures known in integral geometry which provides powerful formulas for the Boolean model. The percolation thresholds of either phase are obtained with good accuracy. From the reconstructions one can subsequently predict property curves for the material across all phase fractions from the single three-dimensional image. We illustrate this for transport and mechanical properties of complex Boolean systems and for experimental sandstone samples.

DOI: [10.1103/PhysRevE.80.051303](https://doi.org/10.1103/PhysRevE.80.051303)

PACS number(s): 81.05.Rm, 61.43.Gt, 47.56.+r

**I. INTRODUCTION**

How do we characterize the structure of a complex two phase material and how do we relate structure to macroscopic physical properties? This question is both of fundamental interest and is crucial to the understanding of many industrially important processes with applications ranging from materials science to geophysics. We addressed this question for the particular class of Boolean composites in a recent publication [1]. Here we provide a more in depth analysis.

Predicting the properties of complex materials relies on the availability of accurate microstructural models, which in turn relies on accurate statistical characterization. Beyond the volume fraction of each phase and the interfacial surface area, the most important statistical quantity has been the two-point correlation function which is obtained from cross-sectional micrographs or small-angle scattering experiments. It is widely recognized that although the two-point correlation function of a reference and a reconstructed system is in good agreement, this does not ensure that the structures of the two systems will match well and attempts to reconstruct materials from experimentally measured two-point information have not been very successful [2,3]. Two point information is nonunique and does not capture many important features of the microstructure. Other useful characterizations of microstructure include the chord-length distribution function [4] (and the related lineal-path function [5]) and the pore size distribution function [6]. Additional accurate descriptors of morphology can be constructed by considering Minkowski functions, e.g., of parallel surfaces [7,8].

Reconstructions of experimental data sets based on the more complex morphological descriptors such as chord-length distribution function (and the related lineal-path function) and pore size distribution [5,9–12] give a better representation of the material structure and accurately predict material properties [13,14]. These reconstructions have been limited however to the same phase fraction as the original image.

Extending the reconstruction schemes to a wide range of phase fractions has not generally been attempted. Studies of complex materials across a large range of phase fractions have been limited to more generic model morphologies. Examples include Boolean models of overlapping particles (see, e.g., [15] and references therein) and Gaussian random-field models [2,3,16,17]. These methods have given important qualitative information on structure or property relationships but cannot be applied directly to a specific material.

The Boolean model is generated by the gradual build up of a phase via the overlap of permeable “grains” (closed and bounded convex shapes) each with arbitrary location and orientation. Although idealized, the model is often used to reconstruct the morphology of complex materials [15]; examples in the literature include ceramic powders [18], wood composites [19], paper [20], sedimentary rock [21,22], and hydrating cement-based materials [23]. In many of these studies the grain size of the matching Boolean model is chosen by either matching two-point information or by choosing some averaged grain size. The latter is often difficult since for most real materials one has incomplete knowledge of the full distribution of grain sizes and shapes.

In this paper we show that one can accurately reconstruct arbitrary complex Boolean systems from analysis of morphological measures given by integral geometry. Integral geometry provides powerful formulas for the Boolean grain model. In particular one can directly relate local morphological properties of the grains to global morphological measures. This allows one to derive, from a single three-

\*c.arns@unsw.edu.au

†mark.knackstedt@anu.edu.au

‡klaus.mecke@physik.uni-erlangen.de

dimensional (3D) image, an equivalent local Boolean grain ensemble. This in turn, allows one to accurately reconstruct the medium for all particulate phase fractions  $f$ . We illustrate this methodology by predicting the percolation threshold of either phase of a complex two-phase Boolean system from a single image. From the reconstructions one can also predict the  $f$  dependence of a range of material properties. Match of the reconstructed system to the original complex material is excellent for both transport and mechanical properties. We illustrate the method for a complex Boolean system and an experimental sandstone sample.

The plan of the paper is as follows: we review the necessary mathematical background, namely, formulas for calculating the integral geometric measures of Boolean mixtures of lattice grains. In Sec. III we derive local morphological measures from single images of a range of complex Boolean systems. In Sec. IV we generate reconstructions of a complex system, compare the percolation thresholds, and derive the full mechanical and transport properties for general  $\phi$ . In Sec. V we compare different Boolean reconstructions of an experimental image, a (non-Boolean) sandstone, across a range of phase fractions  $\phi$ . We show the match to the mechanical and transport properties of the original image and the different reconstruction strategies.

## II. INTEGRAL GEOMETRY

Integral geometry [24] provides complementary methods and tools for measuring spatial structure. These tools are commonly used in other disciplines (e.g., digital picture analysis [25]) but have only recently been developed as measures of complex media [7,26,27]. A family of measures, the Minkowski functionals in particular, seem to be promising measures for describing the morphology of complex materials. The functionals characterize not only the connectivity but the shape and content of spatial figures. As many physical phenomena depend essentially on the geometry of the spatial structure, integral geometry may provide useful tools to study physical systems. In particular, integral geometry provides powerful formulas for the Boolean model.

We consider a two-component medium filling a cubic volume  $V=L^3$ . A digitized set of either component can be described by a collection of voxels of compact (closed and bounded) convex sets. The mean values  $v_\nu$  of the global Minkowski functionals of a structure made up of Boolean grains of density  $\rho$  (in units of  $a^{-3}$  and  $a$  is the lattice constant) are [28,29]

$$\begin{aligned} v_0(\rho) &= 1 - e^{-\rho V_0}, \\ v_1(\rho) &= e^{-\rho V_0}(1 - e^{-\rho V_1}), \\ v_2(\rho) &= e^{-\rho V_0}(-1 + 2e^{-\rho V_1} - e^{-\rho(2V_1+V_2)}), \\ v_3(\rho) &= e^{-\rho V_0}(1 - 3e^{-\rho V_1} + 3e^{-\rho(2V_1+V_2)} - e^{-\rho(3V_1+3V_2+V_3)}), \end{aligned} \quad (1)$$

where  $V_\nu(K)$  are the morphological measures of the individual grains  $K$ . The measures  $V_\nu$  are related to the familiar

morphological measures of volume fraction  $V$ , discretized surface area  $S$  (number of plaquettes), integral mean curvature  $H$  (number of signed edges), and Euler characteristic  $\mathcal{X}$  [28] of the individual grain:

$$\begin{aligned} V_0 &= V/a^3, \\ V_1 &= S/(6a^2), \\ V_2 &= H/(3\pi a), \\ V_3 &= \mathcal{X} = 1. \end{aligned} \quad (2)$$

For Poisson distributed cubes of sidelength  $\lambda$  we have  $V_0=\lambda^3$ ,  $V_1=\lambda^2$ ,  $V_2=\lambda$ , and  $V_3=1$ . This powerful formulas illustrates that it is sufficient to know the morphology of the individual grains  $V_\nu$  to derive the mean values of the global morphology,  $v_\nu(\rho)$ , for any  $\rho$ .

This result holds also for complex mixtures of grains where  $V_\nu$  is now replaced by proper averaged values. For mixtures of polyhedra one can replace the quantities  $V_\nu$  of a single grain by averages over an ensemble of  $n$  grains, weighted by the probability  $p_j$  of their occurrence

$$\langle V_\nu \rangle = \sum_{j=1}^n p_j V_{\nu j} \quad \text{for } \nu = 0, \dots, d, \quad (3)$$

where  $p_j = \rho_j / \rho$  is the ratio of the densities of the Poisson process. One may even consider correlated grains and replace  $V_\nu$  by the effective measures

$$V_\nu^{corr}(K) = V_\nu(K) - \frac{\rho}{2} \int d\mathcal{R} \int d\vec{r} V_\nu[K \cap K_{\mathcal{R}}(\vec{r})] \xi(\vec{r}) \quad (4)$$

of the individual grains, where  $K_{\mathcal{R}}(\vec{r})$  denotes the (by the vector  $\vec{r}$ ) translated and rotated grain  $K$  and

$$\xi(\vec{r}_1 - \vec{r}_2) = \frac{\langle \rho(\vec{r}_1) \rho(\vec{r}_2) \rangle}{\langle \rho(\vec{r}_1) \rangle \langle \rho(\vec{r}_2) \rangle} - 1 \quad (5)$$

is the normalized and centered correlation function of the grains, i.e., the distribution of distances  $\vec{r}_1 - \vec{r}_2$  of two grains located at  $\vec{r}_1$  and  $\vec{r}_2$ .

In order to evaluate the influence of curvature on the physical properties of real systems and because of their wide use as models of composites, we consider also spheroidal grains. For discrete (voxelated) spheroids one must carefully consider both discretization errors and projections of the grains onto the planar axes. A detailed discussion of the derivation of equivalent local measures for spheroidal systems is given in the Appendix.

The global Minkowski functionals  $v_\nu(\rho)$  can be measured directly from any image made up of discrete voxels. For example, the volume fraction  $v_0$  of a phase is trivially obtained by dividing the number of voxels of that phase by the total number of voxels. The other functionals are obtained by considering the interface associated with the vertices of each voxel. Global measures for each configuration are obtained by configuration counts over all vertices on any voxelated structure after normalizing by the total number of vertices [26,30,31].

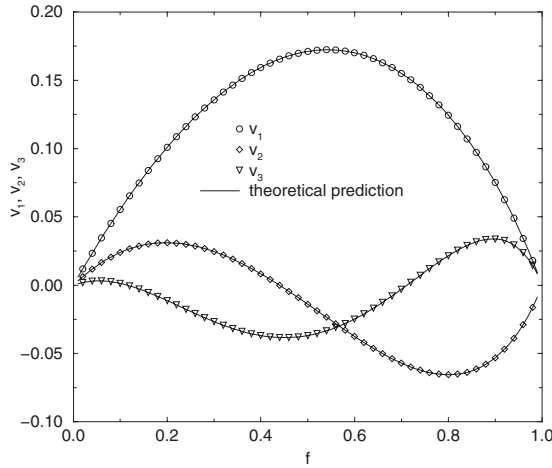


FIG. 1. Minkowski measures over particle fraction for a mixture of cubes and sticks ( $\lambda_{1i}=2$ ,  $\lambda_{21}=8$ ,  $\lambda_{22}=\lambda_{23}=1$ , and  $p_1=1/2$ ).

In [26] the algorithm used to calculate  $v_\nu$  was validated against Eq. (1) for a monodisperse grain ensemble. To further validate the algorithm we measure the global MFs  $v_\nu(\rho)$  for an ensemble made up of mixtures of grains. For each of these mixtures the MFs were computed on a minimum lattice size of  $200^3$  for a minimum of 50 realizations over the full range of the volume fraction  $\phi$  in steps of  $\Delta\phi=0.02$ . Figure 1 illustrates the results; for a system made up of a mixture of cubes ( $2^3$ ) and sticks ( $8 \times 1 \times 1$ ) with  $p=1/2$  we observe agreement between the theoretical and computational results.

### III. DERIVATION OF LOCAL MORPHOLOGICAL MEASURES

To date we have used knowledge of the local “grain” morphology to predict global morphology of a Boolean process [26,28]. Here we show that one can also do the inverse; from a single snapshot of a complex Boolean process one can derive the equivalent local grain morphology of the process defined by  $\langle V_\nu \rangle$ . For all Boolean models made up of compact grains  $\langle V_3 \rangle = 1$ . As one can evaluate the four global measures  $v_\nu$  from a single 3D image, one can use Eq. (1) to directly solve for  $\langle V_0 \rangle$ ,  $\langle V_1 \rangle$ ,  $\langle V_2 \rangle$ , and Poisson density  $\rho$ . We illustrate this first for Boolean samples made up of monodisperse grains.

#### A. Homogeneous Boolean mixtures

We generate realizations of Poisson distributed cubes of different length ( $\lambda=1, \dots, 16$ ) for a range of phase fractions on lattices of  $200^3$  and  $400^3$ . From the image we determine the global measures  $v_\nu$  for different values of  $f$  and from Eq. (1) evaluate the equivalent local measures for that image,  $\rho_{im}$  and  $V_\nu^{im}$ . In Table I we compare  $\rho_{im}, V_\nu^{im}$  to the exact values for two specific systems using the norm of the relative error

$$E_\nu = \frac{\|V_\nu^{im} - V_\nu\|}{V_\nu}. \quad (6)$$

In all cases the densities and the local measures vary little from the analytic results.

Remarkably, even at high volume fractions where most grains overlap and resolving the local grain ensemble is difficult, the predictions of the local measures are still good ( $<2\%$  error).

We further consider a system of identical Poisson distributed spheres. As described in the Appendix, the exact local measures of discretized spheres of radius  $r$  do not coincide with their continuum counterparts. Exact values for the local  $v_\nu$  are given in Table II along with their prediction from single digitized images at different  $f$ . As with the systems of cubes the resultant local measures  $V_\nu^{im}$  are in excellent agreement over all  $f$ .

#### B. Heterogeneous Boolean mixtures

We now generate a very heterogeneous isotropic mixture of five polyhedra (5-mix): a system made up of sticks ( $40 \times 1 \times 1$ ), plates ( $20 \times 20 \times 1$ ), cubes ( $8 \times 8 \times 8$ ), and two other rectangular prisms ( $10 \times 5 \times 2$ ) and ( $16 \times 8 \times 4$ ) in the ratio 10%:10%:40%:20%:20%. The analytic local measures derived from Eq. (3) are given in Table III along with estimates  $V_\nu^{im}$  obtained from a single snapshot of the mixture at  $L=500$  for different  $f$ . The error in the local measures is again very small despite the complexity of the mixture. This indicates that one can define an equivalent local “grain ensemble” from a single 3D snapshot of an extremely complex material.

#### C. Error in morphological measures

In Tables I–III we note that at high particle densities, where most particles overlap, the estimation of the local measures  $\langle V_\nu \rangle$  is less accurate. At higher phase fractions one may need to consider larger sampling volumes ( $L$ ) to obtain accurate predictions. Since we wish to characterize the local  $\langle V_\nu \rangle$  from a single 3D image, we quantify the standard deviation  $\sigma(L)$  of the measures  $V_\nu^{im}$  as a function of image size  $L$  and analyze the scaling of the standard deviation; analytically it has been shown that  $\sigma(L) \approx L^{-3/2}$  [32]. We plot  $\sigma(L)$  for Boolean models of cubes ( $\lambda=8$ ) and spheres ( $r=4$ ) at three different particle fractions  $f$  in Fig. 2.

We note that the standard deviations increase with  $f$  and observe the analytical scaling behavior for all local measures. For reasonably large images,  $L \geq 400$ , about 50 times larger than the grain size,  $\sigma(L)$  is  $\leq 1\%$ . At these resolutions one would therefore expect to accurately define an equivalent grain ensemble. Accurate reconstruction techniques for complex morphologies have long been sought. Given that microcomputed tomographic imaging techniques can now produce images at scales of  $>500^3$  voxels one should be able to define equivalent local grain information from experimental images.

### IV. PROPERTIES OF EQUIVALENT BOOLEAN STRUCTURES FOR ALL FRACTIONS

Having accurately derived the equivalent grain ensemble defined by  $V_\nu^{im}$  from a single image at any  $f$  one can use this to reconstruct statistically equivalent complex materials. In the simplest case one might derive an equivalent rectangular

TABLE I. Local morphological measures for systems of Poisson distributed cubes at  $\lambda=4$  ( $L=200$ ) and  $\lambda=8$  ( $L=400$ ). The first row (labeled exact) gives the analytical values for the local  $V_\nu$ ; the subsequent rows give the prediction of  $V_\nu^{im}$  from the measurement of  $v_\nu$  and use of Eq. (1) for different  $\rho$ .  $\rho$  in the table is the analytic Poisson density from Eq. (1) and  $\rho_{im}$  gives the density measured from the images.

$\lambda=4$					
	$V_0$	$V_1$	$V_2$		
Exact	64	16	4		
$f$	$E_0$ (%)	$E_1$ (%)	$E_2$ (%)	$\rho$ ( $10^{-3}$ )	$\rho_{im}$
0.2000	0.090	0.079	0.060	3.529	$3.486 \times 10^{-3}$
0.5000	0.157	0.159	0.143	10.92	$10.83 \times 10^{-3}$
0.8000	0.291	0.308	0.342	25.56	$25.14 \times 10^{-3}$
$\lambda=8$					
	$V_0$	$V_1$	$V_2$		
Exact	512	64	8		
$f$	$E_0$ (%)	$E_1$ (%)	$E_2$ (%)	$\rho$ ( $10^{-3}$ )	$\rho_{im}$
0.1000	0.158	0.132	0.089	0.2076	$2.058 \times 10^{-4}$
0.2000	0.106	0.110	0.117	0.4340	$4.359 \times 10^{-4}$
0.3000	0.003	0.008	0.030	0.7031	$6.969 \times 10^{-4}$
0.4000	0.097	0.094	0.085	0.9917	$9.980 \times 10^{-4}$
0.5000	0.084	0.093	0.093	1.376	$1.354 \times 10^{-3}$
0.6000	0.101	0.128	0.117	1.818	$1.790 \times 10^{-3}$
0.7000	0.001	0.025	0.048	2.311	$2.352 \times 10^{-3}$
0.8000	0.456	0.413	0.273	3.195	$3.143 \times 10^{-3}$
0.9000	1.91	1.82	1.47	4.486	$4.496 \times 10^{-3}$

TABLE II. Local morphological measures of systems of Poisson distributed spheres at  $r=4$  (top) and  $r=8$  (bottom) on a  $200^3$  lattice. The theoretical values of the single grains in the first lines are for discretized spheres.

$r=4$					
	$V_0$	$V_1$	$V_2$		
Exact	251	45	7		
$f$	$E_0$ (%)	$E_1$ (%)	$E_2$ (%)	$\rho$ ( $10^{-3}$ )	$\rho_{im}$
0.2000	0.523	0.491	0.397	0.8709	$8.893 \times 10^{-4}$
0.5000	0.333	0.295	0.160	2.801	$2.762 \times 10^{-3}$
0.8000	0.683	0.669	0.476	6.594	$6.417 \times 10^{-3}$
$r=8$					
	$V_0$	$V_1$	$V_2$		
Exact	2103	193	15		
$f$	$E_0$ (%)	$E_1$ (%)	$E_2$ (%)	$\rho$ ( $10^{-4}$ )	$\rho_{im}$
0.2000	0.010	0.574	0.427	0.9584	$1.060 \times 10^{-4}$
0.5001	1.12	1.15	1.20	3.441	$3.295 \times 10^{-4}$
0.8000	2.55	1.98	2.47	8.076	$7.651 \times 10^{-4}$

TABLE III. Local morphological measures of the five-mix system of 10% sticks ( $40 \times 1 \times 1$ ), 10% plates ( $20 \times 20 \times 1$ ), 40% cubes ( $8 \times 8 \times 8$ ), 20% each of rectangular prisms of size ( $10 \times 5 \times 2$ ) and ( $16 \times 8 \times 4$ ) on a  $500^3$  lattice. The theoretical values of the mixture are given in the first line, the others are the predictions from the simulations taken at different particle fractions  $f$ .

	$V_0$	$V_1$	$V_2$	
Analytic	371.2	$63.2\bar{3}$	$8.96\bar{6}$	
$f$	$E_0$ (%)	$E_1$ (%)	$E_2$ (%)	$\rho_{im}$
0.2000	0.089	0.075	0.049	$5.731 \times 10^{-4}$
0.5000	0.075	0.121	0.213	$1.754 \times 10^{-3}$
0.8000	0.472	0.450	0.188	$4.405 \times 10^{-3}$

prism with sidelengths  $\lambda_1, \lambda_2$  and  $\lambda_3$  that match the observed  $V_v^{im}$ . For example, a Boolean model with a grain defined by a rectangular prism with ( $\lambda_1=17.047, \lambda_2=6.516,$  and  $\lambda_3=3.341$ ) is equivalent to the heterogeneous five-mix system at  $\phi=0.50$  ( $V_0^{im}=371.1, V_1^{im}=63.26,$  and  $V_2^{im}=8.967$ ). How-

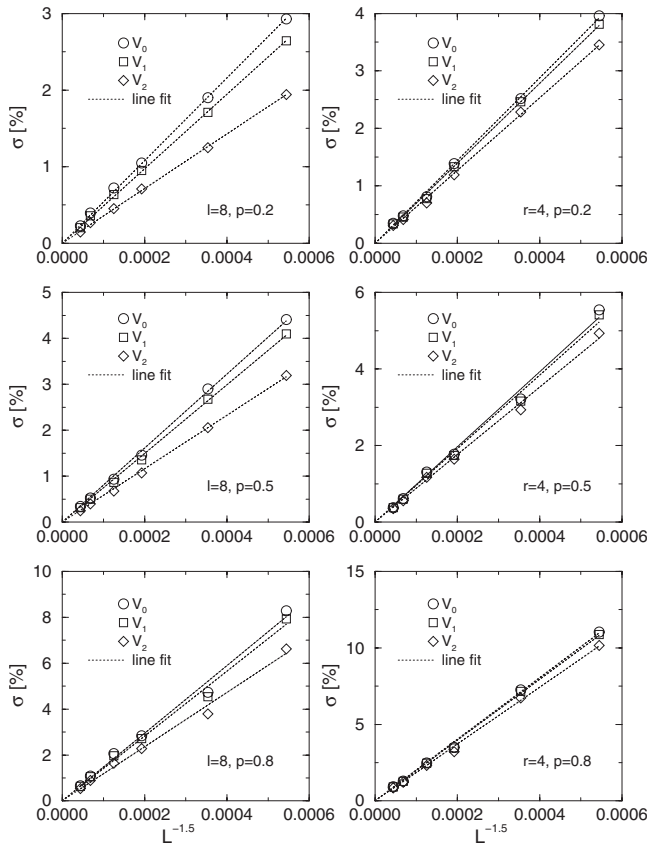


FIG. 2. Scaling of the standard deviation  $\sigma(L)$  of the local measures  $V_v$  for Boolean models with cubes of  $\lambda=8$  (left) and spheres of  $r=4$  (right). Data points are from right to left for  $L=150, 200, 300, 400, 600,$  and  $L=800$ . We show the scaling fit with the theoretical scaling  $L^{-1.5}$ . One obtains a very low standard deviation in the local measures from images measured at large  $L$ . Top:  $f=0.2$ , middle:  $f=0.5$ , and bottom:  $f=0.8$ . Each data points represents at least 100 realizations.

TABLE IV. Match of the equivalent Boolean model to the five-mix system. The norm of the relative errors in the local measures [Eq. (6)] are given. To accurately match the morphology one must consider a two-particle system.

Model	Mixture	$E_v$
$BG^1$	$23 \times 4 \times 4$	$E_0=0.86\%$
Single Boolean grain		$E_1=5.43\%$ $E_2=15.2\%$
$BG^2$	$84.2\%:17 \times 6 \times 2$	$E_0=0.026\%$
Two Boolean grain	$15.8\%:18 \times 14 \times 5$	$E_1=0.040\%$ $E_2=.0041\%$

ever, to generate equivalent Boolean models on a lattice we must generate mixtures of structures with integral  $\lambda_{ji}$ . The best match of a single equivalent Boolean voxelated “grain” to the five-mix system ( $\lambda_1=23, \lambda_2=4,$  and  $\lambda_3=4$ ) however gives a poor match to the  $V_v^{im}$  (Table IV). We therefore obtain the best two-grain match to the observed  $V_v^{im}$ . To do this we consider the local measures of possible combinations of two grains with  $\lambda \in [1; 50], \lambda_1 \geq \lambda_2 \geq \lambda_3$ . The equivalent two-Boolean-grain match ( $BG^2$ ) is defined in Table IV. The morphology of the  $BG^2$  model closely matches the original five-mix system according to the Minkowski functionals. Figure 3 depicts realizations of the Boolean original mixture and its reconstructions for two-particle fractions. As additional morphological measure we calculate the pair volume-volume correlation function given as convolution of the characteristic function  $\chi$  of the microstructure, with  $\chi=1$  for all voxels covered by a particle, and  $\chi=0$  for all void voxels:

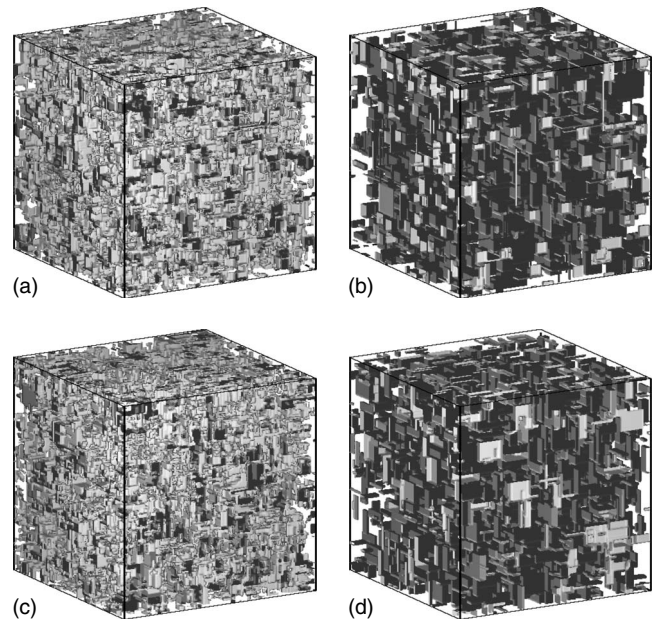


FIG. 3. Original five-mix system of 10% sticks ( $40 \times 1 \times 1$ ), 10% plates ( $20 \times 20 \times 1$ ), 40% cubes ( $8 \times 8 \times 8$ ), 20% each of rectangular prisms of size ( $10 \times 5 \times 2$ ), and ( $16 \times 8 \times 4$ ) on a  $500^3$  lattice at (a) 20% and (b) 80% grain fraction and (c) and (d) corresponding two-particle reconstructions.

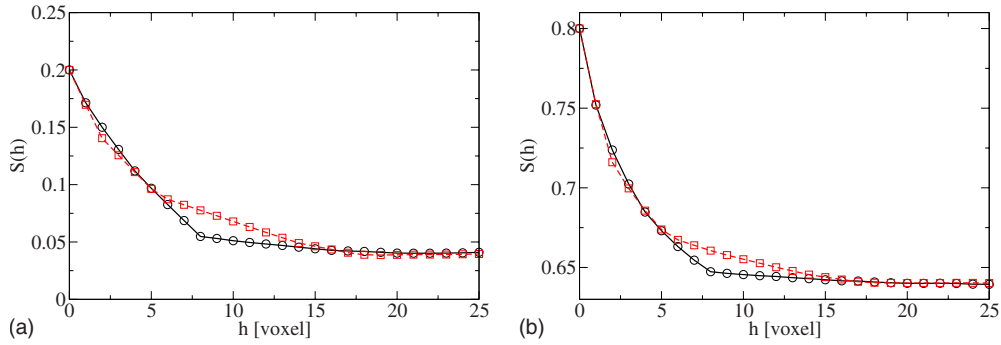


FIG. 4. (Color online) Comparison of the correlation functions of the original five-grain mixture (shown as spheres) of 10% sticks ( $40 \times 1 \times 1$ ), 10% plates ( $20 \times 20 \times 1$ ), 40% cubes ( $8 \times 8 \times 8$ ), 20% each of rectangular prisms of size ( $10 \times 5 \times 2$ ) and ( $16 \times 8 \times 4$ ) to the two-grain reconstruction ( $BG^2$ , shown as cubes) given in Table IV for particle fractions of (a) 20% and (b) 80%.

$$S(h) = \frac{1}{N} \sum_{h_{ij}=h} \chi(\vec{r}_i) \chi(\vec{r}_j), \quad (7)$$

where  $h_{ij} = \|\vec{r}_i - \vec{r}_j\|$  is the distance between a pair of points at locations  $r_i$  and  $r_j$  and the sum runs over all  $N$  pairs of points (voxel) at  $h_{ij}=h$ . A comparison of the two-point correlation functions of the original mixture and its reconstruction is given in Fig. 4.

Having defined an equivalent voxelated Boolean grain ensemble, the question remains; does this equivalent system exhibit similar *physical properties* to the original system? To investigate this we compare the percolation, transport, and mechanical properties of the original five-mix and equivalent  $BG^2$  Boolean system.

### A. Prediction of percolation thresholds

An important test for any microstructural model used to describe transport and mechanical properties of random materials is the ability to estimate the percolation threshold  $p_c$  as a function of volume fraction. Rough bounds on the percolation threshold of polydisperse systems have been derived [33] based on excluded volume arguments, where  $0.084 \leq v_c \leq 0.295$  for continuum percolation in 3D. Accurate estimation of the percolation thresholds for arbitrary complex materials is primarily based on numerical simulations coupled with the knowledge of the size, shape, and orientation of the grains in the original ensemble [34]. However, for most real random materials (e.g., cements, sedimentary rocks, etc.) one has no knowledge of the full distribution of grain sizes and shapes. Here we show that the equivalent grain model derived from the single 3D snapshot allows us to obtain a good estimate of  $p_c$  of the original model.

We vary the density of the original five-mix system defined in Table III and the equivalent  $BG^2$  ensemble given in Table IV and numerically determine the percolation thresholds for both phases of the two models. For the determination of the percolation threshold  $p_c$  of either phase we use finite-size scaling techniques [35], measuring the size dependent  $p_c(L)$  for various  $L$  and using the ansatz:  $p_c = p_c(L) + aL^{-b}$ . The number of realizations was dependent on the sample volume; in general the number of realizations was chosen to obtain  $p_c(L)$  to within a standard error of  $10^{-4}$ . As

an example, for a large lattice ( $L=400$ ), 30 realizations were required, compared to  $3 \times 10^6$  realizations for  $L=10$ . Results are summarized in Table V.

The error in the predictions of  $p_c$  for the equivalent stochastic model is  $\approx 0.3\%$  for the particulate phase and  $\approx 1\%$  for the inverse phase. This ability to closely predict  $p_c$  of *either* phase from one 3D image at *any* phase fraction underlines the power of a morphological characterization and reconstruction based on the integral geometric measures for Boolean models.

### B. Prediction of transport properties

The ability to accurately reconstruct the morphology of complex two-phase materials across the full density range of grains also allows us to generate the full property curves for the material for all phase fractions. We illustrate this for the transport and mechanical properties of the complex five-mix system and its Boolean equivalent.

The conductivity calculation is based on a solution of the Laplace equation with charge conservation boundary conditions. The three-dimensional voxel microstructure is first converted into a network of resistors by connecting each pair of adjacent pixels by a resistor. The conductivity of the local bonds are assigned via the field average method given in [16]. A potential gradient is then applied diagonally across the sample and the system is relaxed using a conjugate gradient technique to evaluate the field. We consider grids sizes of  $150^3$  and compare results at the same scale [16,17,36].

We compare the effective conductivity  $\sigma_e$  of the five-mix system with the equivalent  $BG^2$  model at both infinite contrast  $\sigma_1 : \sigma_2 = 0 : 1$  and  $1 : 0$  and at finite contrast  $\sigma_1 : \sigma_2 = 10 : 1$  and  $1 : 10$ , where  $\sigma_1$  is the conductance of the grain phase. In Fig. 5 we summarize the results. The match of the equivalent

TABLE V. Comparison of the percolation thresholds for the complex five-mix model and its matching Boolean model defined in Table IV.

Phase	$p_c^{original}$	$p_c^{stochastic}$
Particulate	0.143	0.146
Inverse	0.112	0.100

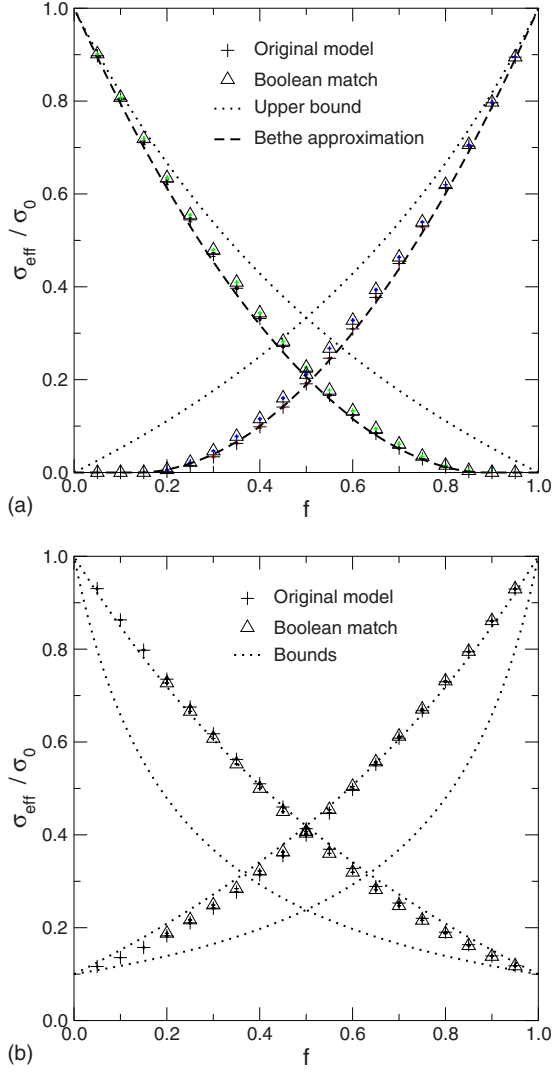


FIG. 5. (Color online) Effective conductivity over fraction  $f$  for the original five-particle mixture given in Table III compared to its equivalent two-grain Boolean model defined in Table IV. The equivalent model defined from the single 3D image at  $f=50\%$  matches the full  $f$ -conductance curve for *both* phases. Top: conductivity grain:pore contrasts 1:0 and 0:1. Bottom: conductivity contrasts 1:0.1 and 0.1:1.  $\sigma_0$  is the larger conductivity of the constituent materials

Boolean model to the original five-mix system is excellent in all cases. For comparison, conventional two-point Hashin-Shtrickman bounds [37] are shown in the figure. Even at infinite contrast, where accurate matches are notoriously difficult, the result is excellent. It is remarkable that from the equivalent  $BG^2$  reconstruction one can generate the conductance curve across all phase fractions from a single image of the original heterogeneous five-mix system. Clearly the morphology of the equivalent Boolean model captures the important structural aspects affecting the conductivity of the two-phase medium in the original image.

Calculation of the full conductivity curve via reconstruction and numerical simulation over a range of phase fractions requires significant computational resources. A much simpler estimation of the conductivity can be derived from the solu-

tion for the microscopic conductivity  $\sigma_m$  of a Bethe lattice [38–40] with the same  $p_c$  as the complex material. The value of  $p_c$  for a Bethe lattice of coordination number  $z$  is  $p_c = 1/(z-1)$  and the exact solution of the microscopic electrical conductance  $\sigma_m$  on the Bethe lattice is given in [41] as well as a set of explicit formulas for binary mixtures ( $\sigma_1 = 1$  and  $\sigma_2 = 0$ ) used here (i)  $p \leq p_c$ , (ii)  $p$  close to 1, (iii)  $p$  close to  $p_c$ , and (iv) conductivity at high coordination number  $z$

$$\sigma_i = 0, \quad (8)$$

$$\sigma_{ii} \approx \frac{z(z-2)}{z-1} \sigma_1 \left[ 1 - c \left\{ 1 + (1+p_c) \sum_{n=2}^{\infty} \frac{p_c^{n-1}}{1+p_c^{2n-1}} \right\} \right], \quad (9)$$

$$\sigma_{iii} \approx 0.761 \frac{2z}{z-2} \sigma_1 \left( \frac{p-p_c}{p_c} \right)^2, \quad (10)$$

$$\sigma_{iv} \approx -z \sigma_1 \sum_{n=0}^4 G_n, \quad \text{where}$$

$$G_0 = -\Delta_p,$$

$$G_1 = 0,$$

$$G_2 = \frac{p_c^2}{p^2} \Delta_p c,$$

$$G_3 = \frac{p_c^3}{p^5} \Delta_p^2 c [p(2p-1) + 3\Delta_p c],$$

$$G_4 = \frac{p_c^4}{p^6} \Delta_p^2 c \left[ 3c^2 \Delta_p - 2pc + \Delta_p(1-3p+3p^2) + 5\Delta_p^2 c \frac{2p-1}{p} + 15\Delta_p^3 c^2 \frac{1}{p^2} \right], \quad (11)$$

and  $c = 1-p$ ,  $\Delta_p = p-p_c$ . The solution was obtained as an interpolation between the different approximations

$$\sigma = \begin{cases} 0 & p \leq p_c \\ \frac{p}{p_c} \sigma_{iii} + \left(1 - \frac{p}{p_c}\right) \sigma_{iv} & 1 \leq \frac{p}{p_c} \leq 1.1 \\ (1-p^2) \sigma_{iv} + p^2 \sigma_{ii} & \frac{p}{p_c} > 1.1. \end{cases} \quad (12)$$

From the average conductivity of the network  $\sigma$  the microscopic conductance  $\sigma_m$  was calculated as

$$\sigma_m = \frac{z-1}{z^2-2z} \sigma. \quad (13)$$

For site based disorder one equates the microscopic conductance to the macroscopic effective prediction of the material  $\sigma_{\text{eff}}$  via

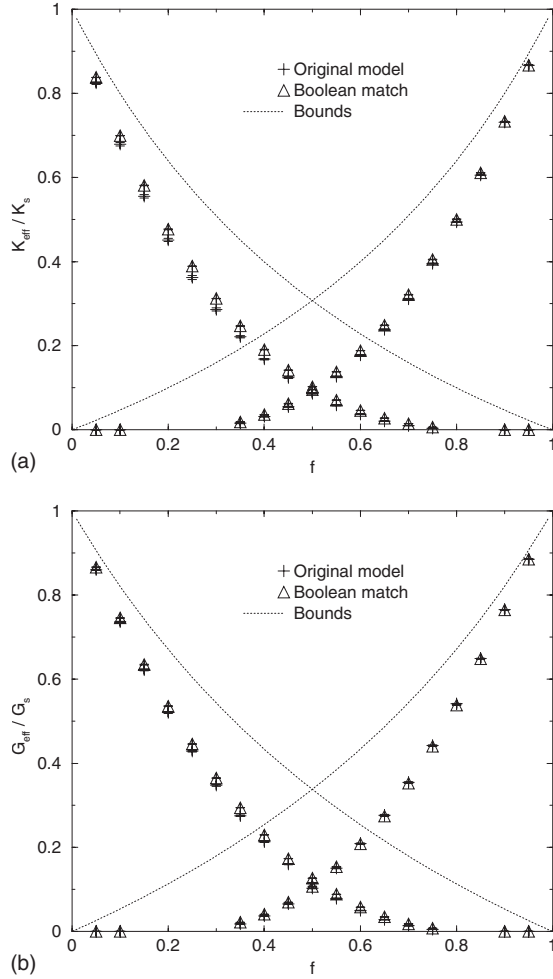


FIG. 6. Bulk and shear modulus over solid grain fraction  $f$  for the heterogeneous five-particle mixture defined in Table III compared to the  $BG^2$  model with equivalent local measures  $V_v$ . The elasticity contrasts are 1:0 and 0:1 for the Young modulus. The Poisson's ratio of the solid phase is set to  $\nu_s=0.25$  in both cases.

$$\sigma_{\text{eff}} = \sigma_m p, \quad (14)$$

where only a fraction  $\approx p$  is conductive on the interface of the domain. This assumes that the total conductive fraction is comparable to the effective conductive fraction. The match of this empirical fit to the data shown in the upper Fig. 5 is excellent.

### C. Prediction of mechanical properties

We use a finite element method (FEM) to estimate the elastic properties of the model system. FEM uses a variational formulation of the linear elastic equations and finds the solution by minimizing the elastic energy via a fast conjugate gradient method. Each voxel is taken to be a trilinear finite element. A homogeneous strain is applied, with the average stress or the average elastic energy giving the effective elastic modulus. Further details of the theory and the programs can be found elsewhere [23,42,43]. In Fig. 6 we show the simulation results for the original five-mix and the equivalent  $BG^2$  match. The agreement is excellent for both 1:0 and 0:1

contrasts [44]. Again the morphology of the equivalent Boolean model captures the structural aspects which effect the mechanical properties of the two-phase material.

## V. EQUIVALENT BOOLEAN MODEL OF A SANDSTONE

Having illustrated the ability of the method to reconstruct complicated Boolean models, we now attempt to accurately reconstruct experimental 3D microtomographic images of sandstone cores. We note that the microstructure of a sandstone is a result of a complex physical process which can include consolidation, compaction and cementation of an original grain packing. More complex and realistic models of sandstones have been derived [45,46]. These methods require however, the simulation of the generating process including primary grain sedimentation followed by a diagenetic process such as compaction and cementation. This process is both computationally expensive and requires several fitting parameters. Reconstructing the microstructure of sandstones by a simplistic Boolean model may therefore not lead to the excellent match observed in the previous section. However, a Boolean sphere pack has been proposed as a model which gives a reasonable representation of consolidated sandstone and yields good qualitative information on structure or property relationships. Moreover, other work [21,22,47,48] has shown that the Boolean sphere model gives a very good match to Fontainebleau sandstone data. Here we consider a number of sandstone samples; a suite of homogeneous Fontainebleau sandstone at different porosities and a more heterogeneous cross-bedded sandstone. We compare the reconstructions to three different Boolean models; a sphere pack with matching two-point information, the equivalent Boolean ensemble defined by local morphological measures, and a model based on the probability density of covering spheres [48].

### A. Experimental data sets

The Fontainebleau images were obtained from 4.52 mm diameter cylindrical core samples extracted from four blocks with bulk porosity  $\phi=7.5\%$ , 13%, 15%, 22%. A 2.91 mm length of each core was imaged [49–51]. The reconstructed images have a resolution of 5.7  $\mu\text{m}$  resulting in  $795 \times 795 \times 512$  imaged sections. From the original cylindrical plug we extract a  $480^3$  cubic subset for analysis corresponding to a volume of 20.5  $\text{mm}^3$ . The cross-bedded sandstone image is of a cylindrical plug, with an original image size of  $512 \times 512 \times 666$  at 10  $\mu\text{m}$  resolution. We select a central  $300 \times 300 \times 600$  sample for further analysis. Both images exhibited strong bimodal distributions of x-ray densities; the images were thresholded using a kriging-based thresholding method [52] to give a binary pore-solid image [53,54].

Analysis of each full image gives us a single value for the porosity and therefore little data to compare to stochastic model predictions. However, both samples exhibit reasonably strong heterogeneity in the pore volume fraction. We show in Fig. 7 traces of the porosity for the Fontainebleau sandstone samples. The Fontainebleau data show little directional dependence.

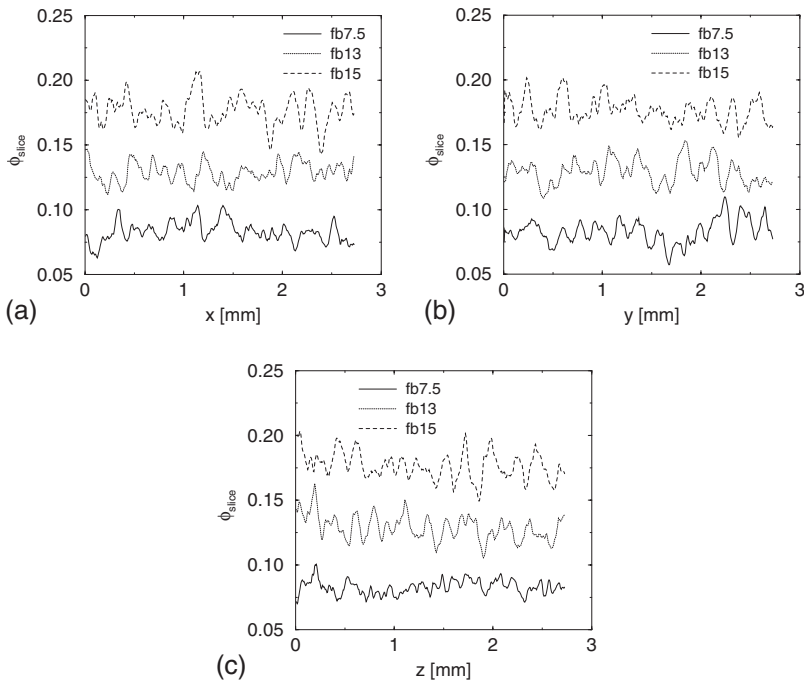


FIG. 7. Variation in the porosity distribution along the  $x$ ,  $y$ , and  $z$  axes for the Fontainebleau sandstone samples of size  $2.7 \times 2.7 \times 2.7 \text{ mm}^3$ . The Fontainebleau sample exhibits negligible directional heterogeneity. Mean of porosity and variance along the  $z$ -direction are for the Fontainebleau samples:  $\phi = 8.29 \pm .54\%$  for fb7.5,  $\phi = 12.9 \pm .95\%$  for fb13, and  $\phi = 17.7 \pm 1.0\%$  for fb15.

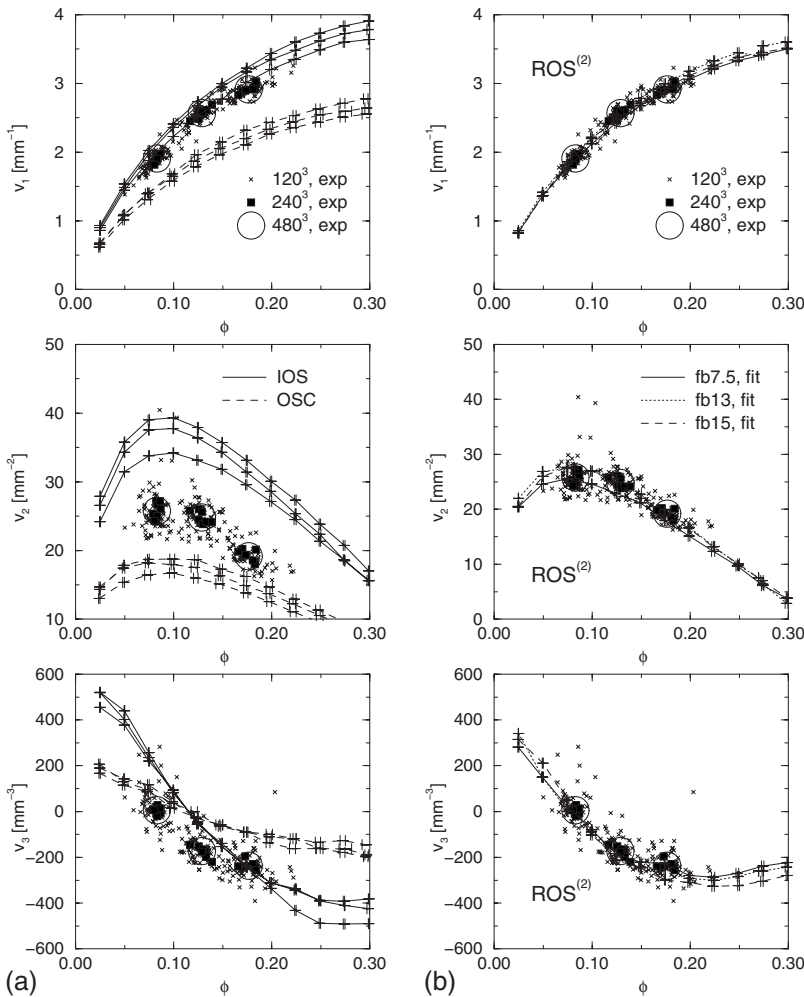


FIG. 8. Global measures  $v_\nu$  of the Fontainebleau sandstone data sets at different image sizes ( $120^3$ – $480^3$ ). The variability in the measures  $v_\nu$  does increase with decreasing image size, but the values at  $120^3$  are consistent with data at the large scale. On the left side we compare the prediction of the IOSC and OSC systems to the  $ROS^2$  model on the right side.

TABLE VI. Local Minkowski measures for the four Fontainebleau sandstone samples (denoted fb $x \cdot y$ , where  $x \cdot y$  is the porosity in percent of the original macroscopic sample)

Sample	$V_0$ ( $10^{-3}$ mm <sup>3</sup> )	$V_1$ ( $10^{-3}$ mm <sup>2</sup> )	$V_2$ (mm)
fb7.5	0.4019	3.994	0.0473
fb13	0.3619	3.752	0.0466
fb15	0.4506	4.520	0.0523
fb22	0.3361	3.965	0.0509

Due to the natural heterogeneity exhibited by sedimentary rock and by appropriately choosing different window sizes on the image we are able to measure morphological parameters for the sandstone plugs across a range of pore volume fractions  $\phi$ . This enables us to more comprehensively compare the experimental images to equivalent Boolean models. For the Fontainebleau samples we consider cubic blocks of  $480^3$ ,  $240^3$ , and  $120^3$  from the full sample volume. This provided in all cases a good spread of porosities across different sampling volumes. The measured morphological properties  $v_\nu(\phi)$  are summarized in Fig. 8. With decreasing sampling volume the variability of the measures increases slightly, but the values are consistent with the data for the larger volumes.

**B. Morphological reconstruction**

In this section we generate the equivalent Boolean reconstructions for the sandstone images based on the two-point correlation function (IOSC model). The correlation function for the phase external to the spheres of radius  $r_0$  in the IOSC model is  $p^{(2)}(r) = p^{(\nu(r))}$  for  $r < 2r_0$  and  $p^{(2)}(r) = \phi^2$  for  $r > 2r_0$  where  $\nu(r) = 1 + \frac{3r}{4r_0} - \frac{r^3}{16r_0^3}$  and  $s/v = -3\phi \ln \phi/r_0$ . The matching sphere radius is given in Table VII.

The equivalent local grain measures  $V_\nu$  are derived via Eq. (1) using the  $v_\nu$  obtained from the four full images of the sandstone samples. Results are summarized in Table VI. We first attempt to fit a single equivalent Boolean grain (IOSB) to this data. The best matching grain model is similar to that obtained by matching to the two-point correlation function. However, as was observed previously for the heterogeneous five-mix system, a single Boolean sphere does not give a good match to the data (Table VIII). By attempting to fit a single equivalent spheroidal grain (ROS<sup>1</sup> model) to the local  $V_\nu$  we see only a slight improvement in the prediction. We therefore define the best two-particle match for Boolean spheroids (ROS<sup>2</sup> model). Values are given in Table VII. The match to the local  $V_\nu$  of the experimental image is now excellent (Table VIII). It is interesting to note that the unique information obtained from the integral geometric measures leads to a quite complex equivalent stochastic model for Fontainebleau sandstone; the ROS<sup>2</sup> model equivalent (Table VII) is composed of two very different particle sizes.

TABLE VII. Parameters for the Boolean models of the Fontainebleau sandstones. The first IOS model (IOS<sup>C</sup>) was matched using the void-void correlation function, the other models are matched using the Boolean reconstruction. All spheroids are randomly oriented (ROS).

Model	Sample	$p_j$	$a$ ( $\mu\text{m}$ )	$b$ ( $\mu\text{m}$ )	$c$ ( $\mu\text{m}$ )
IOS <sup>C</sup>	fb7.5	1	71.3	71.3	71.3
	fb13	1	65.8	65.8	65.8
	fb15	1	69.1	69.1	69.1
	fb22	1	59.0	59.0	59.0
IOS <sup>B</sup>	fb7.5	1	45.8	45.8	45.8
	fb13	1	44.6	44.6	44.6
	fb15	1	47.4	47.4	47.4
	fb22	1	43.2	43.2	43.2
ROS <sup>(1)</sup>	fb7.5	1	48.3	44.9	44.3
	fb13	1	44.9	44.3	43.7
	fb15	1	51.1	49.4	42.6
	fb22	1	43.2	43.2	43.2
ROS <sup>(2)</sup>	fb7.5	0.848	12.5	11.9	8.52
		0.152	83.5	80.7	77.2
	fb13	0.863	15.9	11.4	9.09
		0.137	84.6	76.7	76.1
	fb15	0.794	15.3	12.5	8.52
		0.206	84.6	80.1	76.7
	fb22	0.751	16.5	10.8	8.52
		0.249	74.4	67.0	63.6

TABLE VIII. Errors in the morphological match of the Boolean models to the Fontainebleau sandstone samples.

Model	Sample	$ \Delta V_0 /V_0$	$ \Delta V_1 /V_1$	$ \Delta V_2 /V_2$
IOS <sup>C</sup>	fb7.5	3.4	3.6	2.5
	fb13	2.4	2.6	1.8
	fb15	3.1	3.4	2.5
	fb22	1.6	1.8	1.3
IOS <sup>B</sup>	fb7.5	$5.3 \times 10^{-3}$	0.71	0.022
	fb13	0.016	0.66	$6.8 \times 10^{-3}$
	fb15	$4.1 \times 10^{-3}$	0.058	0.84
	fb22	$2.5 \times 10^{-3}$	0.44	0.67
ROS <sup>(1)</sup>	fb7.5	$8.1 \times 10^{-5}$	0.64	0.91
	fb13	$1.1 \times 10^{-3}$	0.62	0.83
	fb15	$5.0 \times 10^{-4}$	0.57	0.80
	fb22	$2.5 \times 10^{-3}$	0.44	0.67
ROS <sup>(2)</sup>	fb7.5	$1.5 \times 10^{-7}$	$7.5 \times 10^{-6}$	$1.5 \times 10^{-4}$
	fb13	$9.1 \times 10^{-8}$	$5.4 \times 10^{-7}$	$3.0 \times 10^{-5}$
	fb15	$1.8 \times 10^{-7}$	$2.7 \times 10^{-6}$	$8.9 \times 10^{-5}$
	fb22	$2.1 \times 10^{-7}$	$2.0 \times 10^{-6}$	$1.6 \times 10^{-5}$
OSC	fb7.5	7.4	5.2	2.4
	fb13	12	8.6	4.1
	fb15	5.3	3.9	2.0
	fb22	3.2	2.4	1.4

Recently Thovert *et al.* [48] introduced a reconstruction technique based on a Boolean sphere pack for sandstone where the sphere size distribution is defined by the probability density of the covering radius for spheres (OSC model).

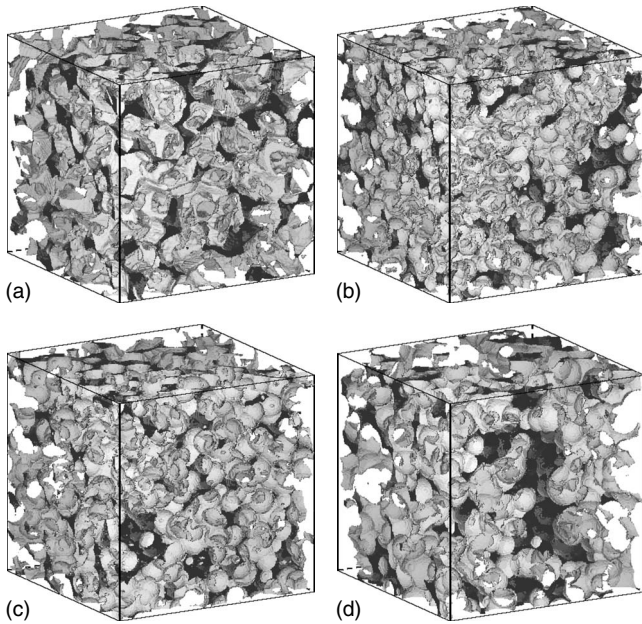


FIG. 9. Visual comparisons of Fontainebleau sandstone reconstructions  $240^3$ ,  $\phi=18.2\%$  to the original data sets. (a) Original sandstone image. (b) reconstruction based on the IOS<sup>C</sup> model. (c) reconstruction based on the ROS<sup>2</sup> model. (d) reconstruction based on the OSC model.

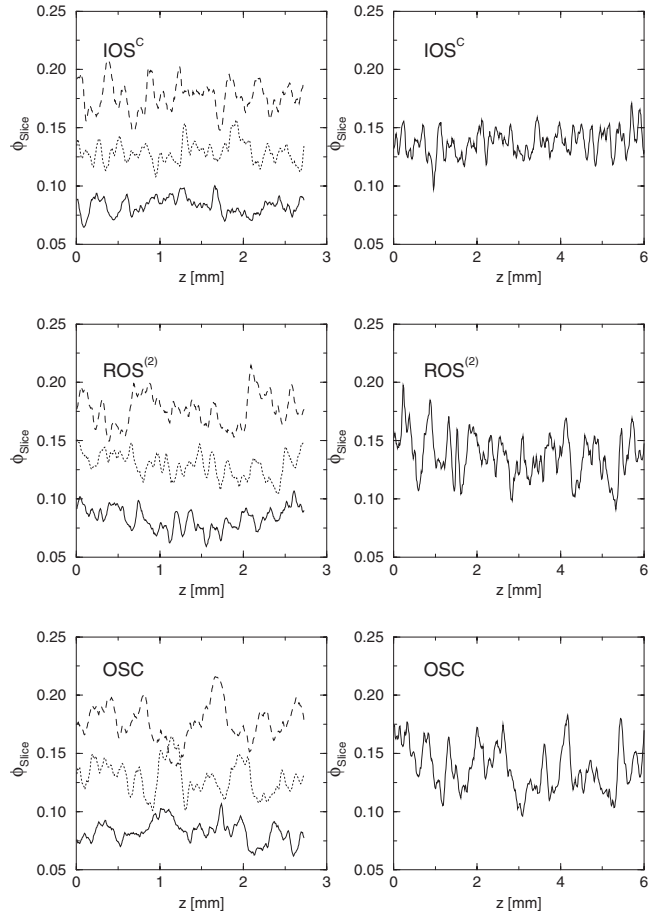


FIG. 10. Variation in the porosity distribution along the  $z$  axis of the Boolean reconstructions to the Fontainebleau sandstone. Sample size is the same as in Fig. 7.

We employ this method to generate a third equivalent Boolean model for the four sandstone images. Details of the analysis and the resultant distributions of covering radius are given in Appendix, Sec. 2.

In Fig. 8 we compare the morphological measures of the IOS<sup>C</sup> model, the ROS<sup>2</sup> model and the OSC model to measures of the original sandstone images. The fit of the ROS<sup>2</sup> model is superior. We now compare the predictions of these three Boolean ensembles for structural, transport, and mechanical properties of the original sandstone images.

### C. Structural, transport, and mechanical properties

The original sandstone microstructure and the matching IOS<sup>C</sup>, ROS<sup>2</sup>, and OSC models are illustrated in Fig. 9 for one subset of the Fontainebleau sandstone suite and for one subset of the crossbedded sandstone sample. Visual inspection suggests that the ROS<sup>2</sup> and OSC models more closely resemble the microtomographic image than the IOS<sup>C</sup> model. In Fig. 10 we illustrate the porosity distributions of the IOS<sup>C</sup>, ROS<sup>2</sup> and OSC reconstructions (compare to Fig. 7). It is difficult to distinguish which reconstruction gives the better match for the Fontainebleau data sets, but the ROS<sup>2</sup> and OSC models better reflect the structure and heterogeneity of the crossbedded sample. In particular, the IOS<sup>C</sup> recon-

structed image clearly does not capture the inherent heterogeneity of the original rock image.

**D. Transport and mechanical properties of reconstructions**

The morphology of the sandstone determines its macroscopic physical properties. We now compare the mechanical and transport properties of the original sandstone data set to the model Boolean reconstructions.

In the conductivity simulations we apply the potential gradient across the  $x$ -,  $y$ -, and  $z$ -axes. As the system is no longer periodic, we consider open boundary conditions on the four faces parallel to the direction of the gradient. We consider an infinite conductivity contrast:  $grain:pore=0:1$  mimicking a measurement of the electrical conductivity of a fluid saturated sample. The conductivity is calculated on images at  $120^3$ . The conductivity of the pore space measured on cells at this scale are in good agreement with simulations on larger grids [55], give a large ensemble of samples (64 per core), and provide a good spread of porosities from each core. This allows us to obtain the conductance curve across a range of porosities from each image (Figs. 11).

The predictions of the model reconstructions are also shown in Figs. 11. All reconstructions do quite well. The OSC reconstruction gives a poor match to the data for the low porosity sample and the IOSC model is poorest for the high porosity sample.

When calculating the elastic properties via FEM, all images are assumed to have periodic boundary conditions. We use the elastic properties of quartz with bulk modulus  $K=37$  GPa and shear modulus  $G=44$  GPa for the solid phase and  $K=G=0$  for the pore space. As with the conductivity simulation, the data exhibit little variability at a cell size of  $120^3$  and one can obtain an elastic modulus-porosity curve from each image [43]. These are shown in Figs. 12 and 13. The results for the elastic properties of the reconstructed morphologies are again in good agreement with data derived directly from the images. For all samples the OSC model gives the worst predictions. The IOSC model matches best for the high porosity Fontainebleau samples, and the  $ROS^2$  model for the low porosity samples. We have noted for the high porosity samples due to the strongly bimodal equivalent grain ensemble in the  $ROS^2$  model that many of the small particles lie “suspended” in the pore space. This unrealistic morphology for sedimentary rock (a consequence of using a Boolean model to model a non-Boolean process) leads to the observed under prediction of the elastic modulus for the  $ROS^2$  model at higher porosities. Methods to condition the matching Boolean ensemble to better mimic real structure are discussed further in the summary section.

**VI. CONCLUSIONS**

The goal of much research in computational materials science is to quantify necessary morphological information and then to develop stochastic models which both accurately reflect the material morphology and allow one to estimate macroscopic properties. We have shown that for the Boolean model of random composite media one can define a set of

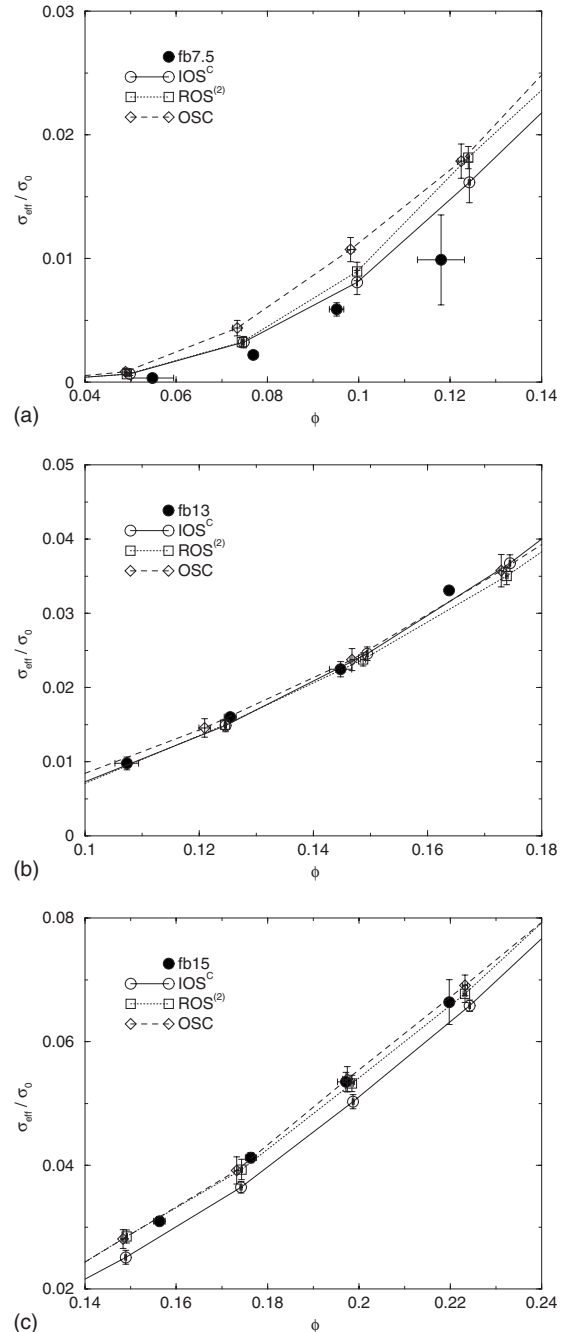


FIG. 11. Comparison of the prediction for conductance of the three matching Boolean models to the Fontainebleau sandstone data. (a) fb7.5, (b) fb13, and (c) fb15. The overlapping sphere model reconstruction (OSC) based on covering radius gives a poor match to the data for the low porosity sample and the identical overlapping sphere model based on reconstruction through the correlation function (IOSC) is poorest for the high porosity sample.

measures from a single image at any phase fraction  $\phi$  which allows one to accurately reconstruct the medium for all other phase fractions. The accuracy of the reconstruction is illustrated by accurately predicting  $p_c$  for the reconstructed data sets and the ability to predict property curves for both conductive and linear elastic properties across all phase fractions.

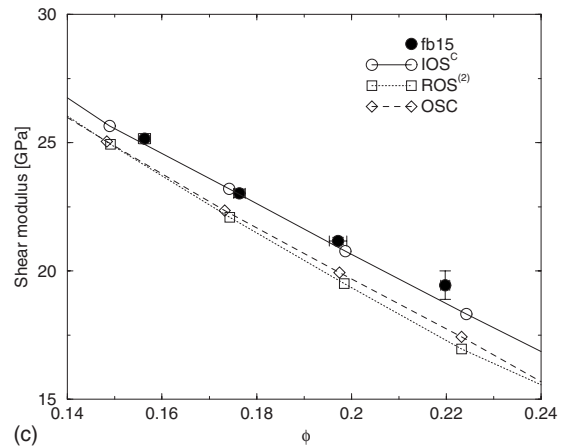
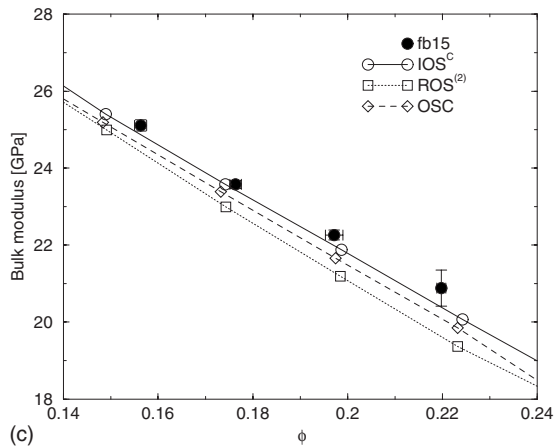
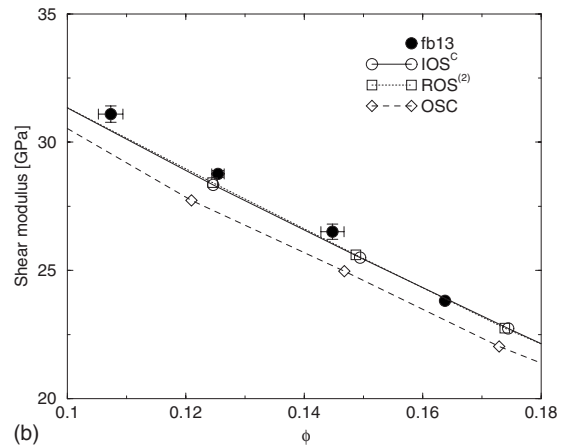
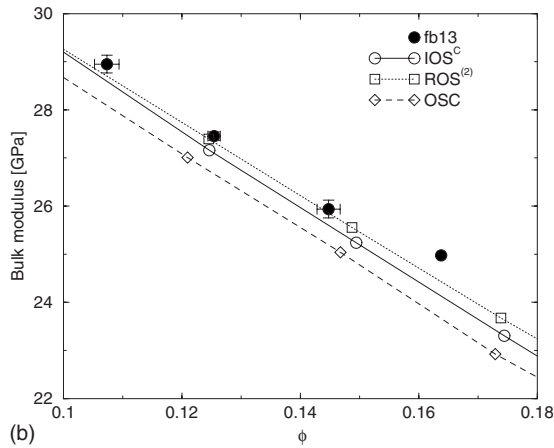
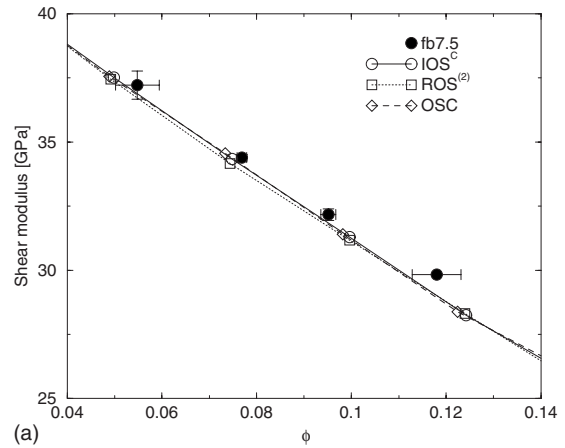
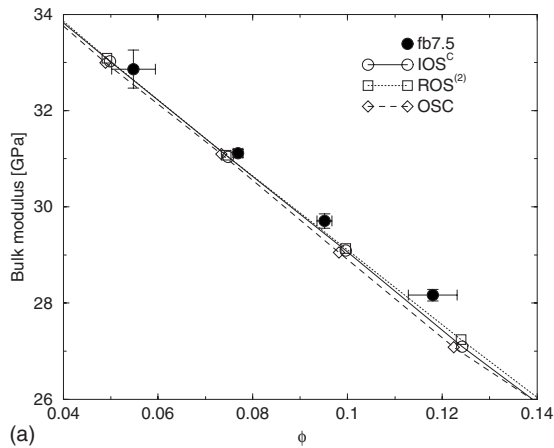


FIG. 12. Comparison of the prediction of the bulk modulus of the matching Boolean models to the water saturated Fontainebleau sandstone data. (a) fb7.5, (b) fb13, and (c) fb15.

FIG. 13. Comparison of the prediction of the shear modulus of the matching Boolean models to the water saturated Fontainebleau sandstone data. (a) fb7.5, (b) fb13, and (c) fb15.

We have illustrated the method for an experimental sandstone image. We show that, in general, the Boolean reconstruction based on integral geometric measures gives a better match to both the morphology and mechanical and transport properties than the commonly used IOSC and the recently developed OSC model. Moreover, unlike the IOSC and OSC models, the current method is not limited to spherical inclusions but can be used to generate more complex inclusion shapes. A development that will further highlight the utility of the proposed technique is based on conditioning the

equivalent ensemble to better mimic the local morphology of the medium. This could be done by conditioning to local curvature measures or chord-length distribution measurements which will limit the choice of grain “shape” to use in the equivalent Boolean ensemble. In oil recovery from petroleum reservoir rocks, an area of particular interest to the authors, recovery depends crucially on the mean curvature of the surfaces where immiscible phases meet at a contact angle. Conditioning an equivalent Boolean ensemble to exhibit the same distribution of local mean curvature should

lead to excellent prediction of multiphase flow properties on reconstructed images.

The current work is based on deriving equivalent local measures from an image for Boolean grain models [Eq. (1)]. Extension of the methodology to more general systems; hard-sphere mixtures, soft sphere models, and models based on Gaussian random fields is now being considered. The further development will enable one to develop accurate reconstructed images for a wide range of complex materials.

In further work we are considering a wider range of complex materials including ceramics, composite materials, and fibrous media.

### ACKNOWLEDGMENTS

C.H.A. and M.A.K. thank the Australian Research Council for financial support. K.R.M. acknowledges support from Deutsche Forschungsgemeinschaft (DFG Grant No. Me1361/7). We thank the Australian National Supercomputing Facility for generous allocations of computer time.

### APPENDIX: CALCULATION OF EQUIVALENT BOOLEAN MODELS

This appendix details the derivation of equivalent Boolean models based on Eq. (3). Explained are subtle points important for calculating the local measures of a grain on the lattice. This is done in two steps, first for lattice oriented polyhedras and then for arbitrarily oriented spheroids.

#### 1. Local measures of oriented prisms

For a random mixture of solid three-dimensional oriented rectangular prisms of sidelengths  $\lambda_{j1}$ ,  $\lambda_{j2}$ , and  $\lambda_{j3}$  all  $n$ -dimensional boundaries of the grains coincide with the lattice. As a result the projections of the grain onto the axes and planes of the (lattice) coordinate system in any of the 6 distinct orientations reflect the intrinsic morphological measures of the grain. Defining  $p_j$  as the probability of the occurrence of a grain by the ratio of the Poisson processes  $p_j = \rho_j / \rho$  of the grains Eq. (3) becomes

$$\begin{aligned} \langle V_0 \rangle &= \sum_{j=1}^n p_j \lambda_{j1} \lambda_{j2} \lambda_{j3}, \\ \langle V_1 \rangle &= \frac{1}{3} \sum_{j=1}^n p_j (\lambda_{j1} \lambda_{j2} + \lambda_{j1} \lambda_{j3} + \lambda_{j2} \lambda_{j3}), \\ \langle V_2 \rangle &= \frac{1}{3} \sum_{j=1}^n p_j (\lambda_{j1} + \lambda_{j2} + \lambda_{j3}), \\ \langle V_3 \rangle &= 1. \end{aligned} \quad (\text{A1})$$

For a single rectangular oriented prism of sidelength  $\lambda_i$  this reads  $\langle V_0 \rangle = \lambda_1 \lambda_2 \lambda_3$ ,  $\langle V_1 \rangle = \frac{1}{3} (\lambda_1 \lambda_2 + \lambda_1 \lambda_3 + \lambda_2 \lambda_3)$ , and  $\langle V_2 \rangle = \frac{1}{3} (\lambda_1 + \lambda_2 + \lambda_3)$ , leading to a cubic equation in  $\lambda$ :

$$\lambda^3 - 3\langle V_2 \rangle \lambda^2 + 3\langle V_1 \rangle \lambda - \langle V_0 \rangle = 0. \quad (\text{A2})$$

In normal form and with  $x = \lambda$  and further  $r = -3\langle V_2 \rangle$ ,  $s = 3\langle V_1 \rangle$ , and  $t = -\langle V_0 \rangle$  this becomes [56]

$$x^3 + rx^2 + sx + t = 0, \quad (\text{A3})$$

which can be written in reduced form [56], using the substitution  $y = x + r/3$ ,  $p = (3s - r^2)/3$ , and  $q = 2r^3/27 - rs/3 + t$ :

$$y^3 + py + q = 0. \quad (\text{A4})$$

Depending on the sign of the discriminant  $D$  the equation has one or three solutions. Here we are only interested in solutions for  $D \leq 0$ , leading to three real solutions and the condition:

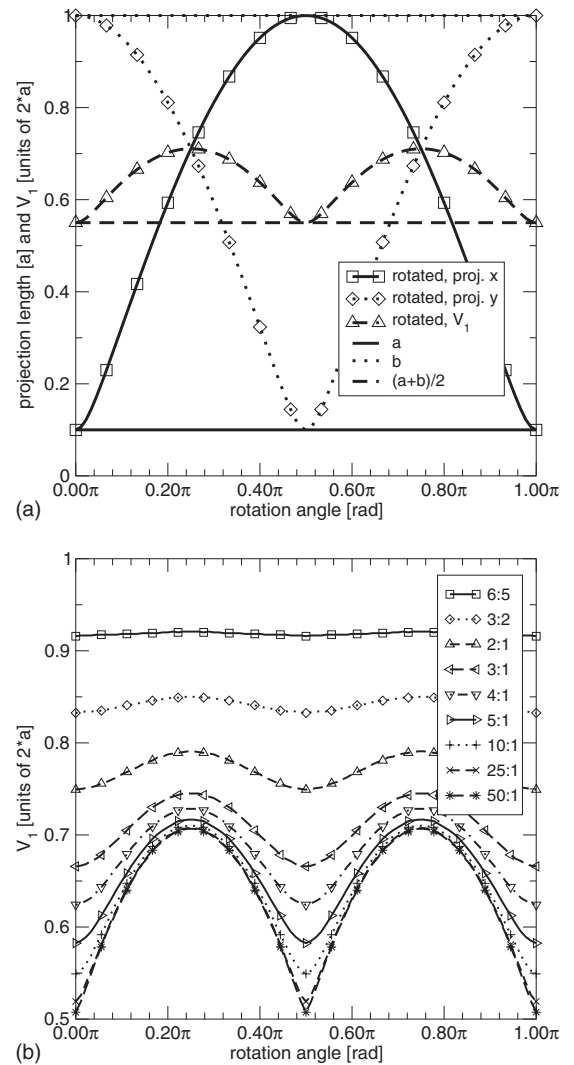


FIG. 14. Illustration of the influence of rotation on the average of the 1D lattice projections of an ellipse with aspect ratio 10:1. (a) Projection length  $V_1$  over rotation angle for an ellipse with aspect ratio of 10:1.  $a$ ,  $b$ , and  $\frac{1}{2}(a+b)$  are given as base cases of the continuum measures. (b) Projection length over rotation angle for ellipses with varying aspect ratios.

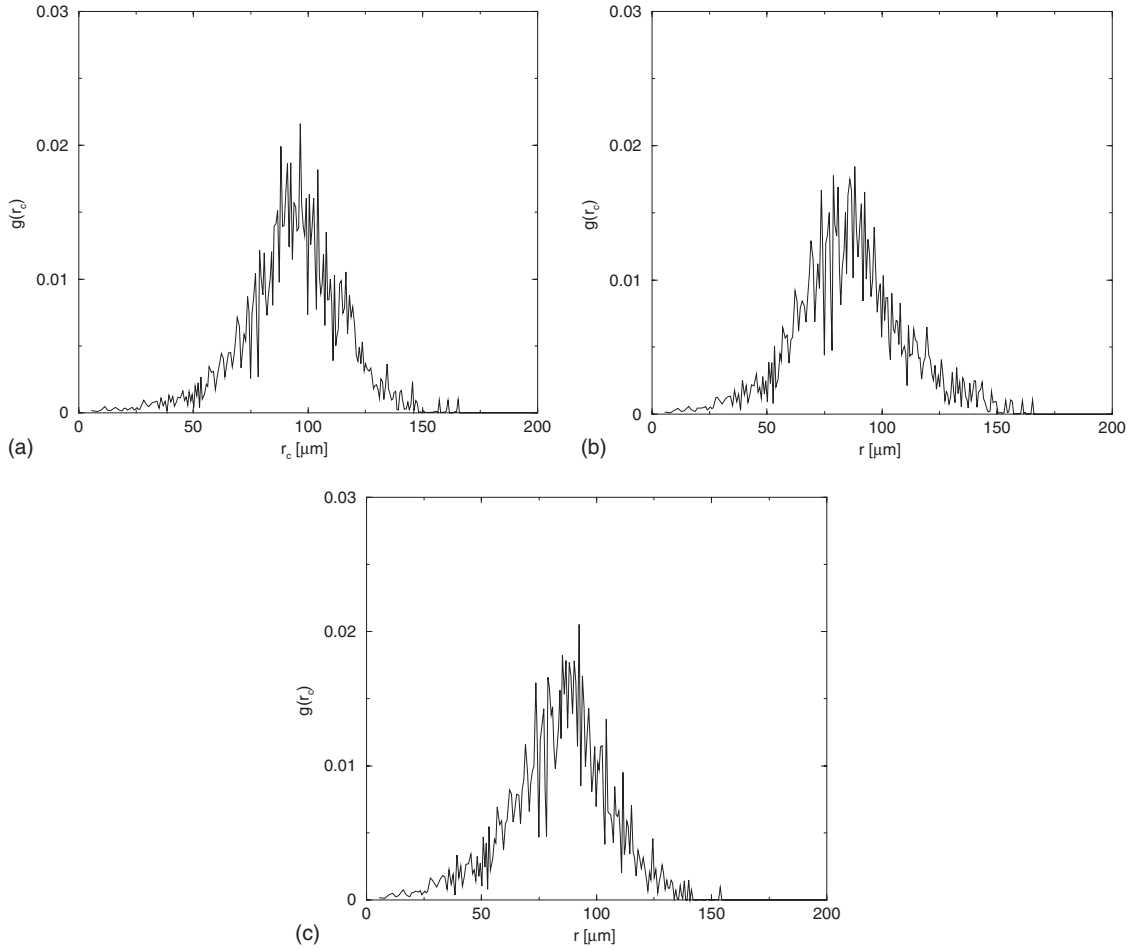


FIG. 15. Probability density of the discretized spheres used for the reconstruction of the sandstone samples (the radius distribution is not evenly spaced). (a) fb7.5, (b) fb13, and (c) fb15.

$$D = \left(\frac{p}{3}\right)^3 + \left(\frac{q}{2}\right)^2 \leq 0. \quad (\text{A5})$$

For  $D=0$  two or three sides of the prism have the same length. The reduced equation is solved using, i.e., the Cardanian formulas [56].

## 2. Local measures of spheroids

Two complications arise in the calculation of the intrinsic measures of the spheroids as considered in this paper. The first is to generalize from lattice oriented grains, which generate an anisotropic structure, to uniform random oriented grains constituting an isotropic structure. The second is the well-known problem of representing curved grains on a cubic lattice.

We start with a system of aligned spheroids. For a lattice oriented spheroid of half-axes  $a, b, c$  the projections of the spheroid into lower dimensional space onto the  $x$ - $y$ ,  $y$ - $z$ , and  $x$ - $z$  planes are ellipses, and onto the  $x, y, z$ —axes are the axes of the spheroid [one-dimensional (1D)], thus giving for the (apparent) local measures in the continuum:

$$\langle V_0 \rangle = \frac{4}{3} \pi abc$$

$$\langle V_1 \rangle = \frac{\pi}{3} (ab + bc + ac)$$

$$\langle V_2 \rangle = \frac{2}{3} (a + b + c)$$

$$\langle V_3 \rangle = 1. \quad (\text{A6})$$

This again leads to a cubic equation which reduces to normal form using  $x=a, b, c$  and further  $r = -\frac{3}{2}\langle V_2 \rangle$ ,  $s = \frac{3}{\pi}\langle V_1 \rangle$ , and  $t = -\frac{3}{4\pi}\langle V_0 \rangle$ . For  $D=0$  ellipsoids or spheres result.

For spheroids not aligned to the lattice coordinate system, the matter becomes more complex. This is illustrated in the following for the two-dimensional case. Taking the  $\langle V_1 \rangle$  measure, the projections of an ellipse onto the axes have different length depending on the rotation angle of the ellipse to the  $x$  axis. To derive the correct  $\langle V_1 \rangle$ , an integration over the rotation angle is necessary. As can be seen in Fig. 14(a),  $V_1 = a + b$  of the aligned system is a lower bound for  $V_1(\theta)$  of a randomly oriented ellipse. Further the upper bound is given by the length of the longer ellipse axis ( $V_1 = 2a$ ). The difference between  $V_1$  for an individual ellipse aligned to the coordinate system as compared to a randomly oriented one is quite substantial for aspect ratios bigger than 2:1 and be-

comes maximal for an ellipse collapsing into a single line ( $b \rightarrow 0$ ), in which case  $V_1(\theta=0)=a$  and  $V_1\theta=\frac{\pi}{4}=\sqrt{2}a$ . Then  $V_1(\theta)$  is given as

$$V_1(\theta) = a(\cos \theta + \sin \theta), \quad (\text{A7})$$

and it follows

$$\langle V_1 \rangle = \frac{a}{\pi} \int_0^\pi (\cos \theta + \sin \theta) d\theta, \quad (\text{A8})$$

where all terms are interpreted as areas, giving  $\langle V_1 \rangle = (4 - 2\sqrt{2})a$ , as compared to  $\langle V_1 \rangle = a$  for the oriented case, a relative difference of about 17%.

In three dimensions only integral equations can be given for the surface of a general spheroid ( $a > b > c$ ) and thus for  $\langle V_1 \rangle$ . Further the image is given at a resolution which does not allow us to use the continuum solution and discretization errors have to be dealt with. We solved this by generating a large lookup table containing all combinations of  $a, b, c$  with  $a \geq b \geq c$  and  $a, b, c \in [1.5; 20]$ ,  $\Delta a = \Delta b = \Delta c = 0.1$ . We integrated numerical over the  $V_v$  at an angle resolution of  $\frac{\pi}{18}$  by generating discrete spheroids and taking the averages. The table can then be searched to find the closest one-particle solution to a given set of intrinsic volumes of a grain.  $N$ -particle solutions can be found equally well by changing the weights in Eq. (3) appropriately.

### 3. Derivation of a Boolean model based on morphological opening

An alternative method of deriving a Boolean model with an imaged based approach was published by Thovert *et al.* [48]. It is based on a morphological opening of the structure with a ball  $B_\lambda$  of radius  $\lambda$  as the structuring element. An opening can be written as a combination of a Minkowski addition or dilation of the domain  $A$  (solid phase in this case), in Thovert's notation [48]

$$A \oplus B_\lambda = \cup_{\mathbf{r} \in A, \mathbf{s} \in B_\lambda} (\mathbf{r} + \mathbf{s}), \quad (\text{A9})$$

and a Minkowski subtraction or erosion of the domain  $A$

$$A \ominus B_\lambda = (A^c \oplus B_\lambda)^c, \quad (\text{A10})$$

giving the opening  $A_{B_\lambda}$  as

$$A_{B_\lambda} = A_\lambda = (A^c \ominus B_\lambda) \oplus B_\lambda. \quad (\text{A11})$$

The procedure for a ball as structuring element is efficiently implemented using a Euclidean distance transformation (the

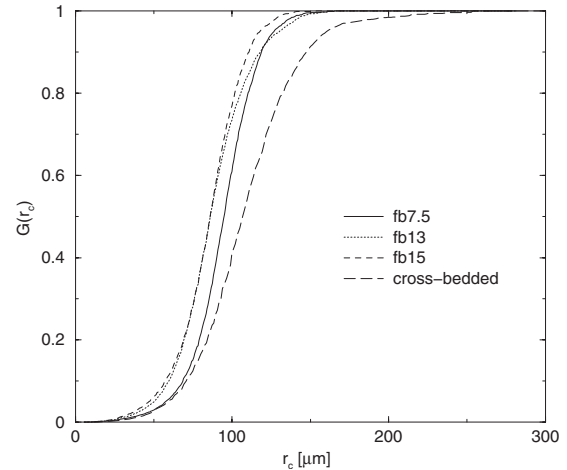


FIG. 16. Radius distribution functions of the discretized spheres used for the reconstruction of the sandstone samples.

square of the Euclidean distance map). We implemented the fast algorithm of Saito [57], which is very fast. By iterating the opening with successively larger radii (by thresholding and recalculating the distance map in every iteration) one can define for each point in  $A$  the radius  $\mathbf{r}_c$  of the largest ball contained in  $A$  that covers  $\mathbf{r}$ . In the language of [48]

$$r_c(\mathbf{r}) = \sup\{\lambda: \mathbf{r} \in A_\lambda\}, \quad (\text{A12})$$

$$A_\lambda = \{\mathbf{r} \in A: r_c(\mathbf{r}) \geq \lambda\}. \quad (\text{A13})$$

The use of the Euclidean distance transform means that the radii of the smallest sphere touching the boundary at a given point in the structure is found rather than the largest inscribed sphere. To stay consistent, the discrete spheres used in the Boolean model are therefore defined as all voxels within a distance  $r$  of the center of the voxel, not including the boundary.

The probability density  $g(r)dr$  of points with radii  $r \leq \mathbf{r}_c < r+dr$  can then be used to generate a Boolean sphere model. For this paper the radii distribution was resolved with a resolution of  $\Delta r \geq 0.1$  voxel, which for a maximal radius of 49.6 voxels gives about 400 different radii. The morphological openings were carried out on the full  $480^3$  Fontainebleau data sets and the resulting radii distributions are shown in Fig. 15.

Alternatively one may use the distribution function  $G$  of the covering radius  $G(r)dr = \int_0^r g(s)ds$ , which is shown in Fig. 16.

- [1] C. H. Arns, M. A. Knackstedt, and K. R. Mecke, Phys. Rev. Lett. **91**, 215506 (2003).  
 [2] P. M. Adler, C. G. Jacquin, and J. A. Quiblier, Int. J. Multiphase Flow **16**, 691 (1990).  
 [3] P. Adler, C. Jacquin, and J.-F. Thovert, Water Resour. Res. **28**, 1571 (1992).  
 [4] *Image Analysis and Mathematical Morphology, Vol. 2: Theo-*

*retical Advances*, edited by J. Serra (Academic, New York, 1992).

- [5] C. L. Y. Yeong and S. Torquato, Phys. Rev. E **57**, 495 (1998).  
 [6] A. Scheidegger, *The Physics of Flow through Porous Media* (University of Toronto Press, Toronto, 1974).  
 [7] C. H. Arns, M. A. Knackstedt, W. V. Pinczewski, and K. R. Mecke, Colloids Surf., A **241**, 351 (2004).

- [8] K. Mecke and C. H. Arns, *J. Phys.: Condens. Matter* **17**, S503 (2005).
- [9] A. P. Roberts, *Phys. Rev. E* **55**, R1286 (1997).
- [10] M. D. Rintoul and S. Torquato, *J. Colloid Interface Sci.* **186**, 467 (1997).
- [11] A. P. Roberts and S. Torquato, *Phys. Rev. E* **59**, 4953 (1999).
- [12] C. Manwart, S. Torquato, and R. Hilfer, *Phys. Rev. E* **62**, 893 (2000).
- [13] A. P. Roberts and E. J. Garboczi, *J. Mech. Phys. Solids* **47**, 2029 (1999).
- [14] S. Torquato, C. L. Y. Yeong, and A. I. Aksay, *J. Am. Ceram. Soc.* **82**, 1263 (1999).
- [15] S. Torquato, *Appl. Mech. Rev.* **44**, 37 (1991).
- [16] A. P. Roberts and M. Teubner, *Phys. Rev. E* **51**, 4141 (1995).
- [17] A. P. Roberts and M. A. Knackstedt, *Phys. Rev. E* **54**, 2313 (1996).
- [18] A. P. Roberts and E. J. Garboczi, *J. Am. Ceram. Soc.* **83**, 3041 (2000).
- [19] H. Wang and S. M. Shaler, *J. Pulp Pap. Sci.* **24**, 314 (1998).
- [20] O. Kallmes, H. Corte, and G. Bernier, *Tappi J.* **44**, 519 (1961).
- [21] L. M. Schwartz, N. Martys, D. P. Bentz, E. J. Garboczi, and S. Torquato, *Phys. Rev. E* **48**, 4584 (1993).
- [22] N. S. Martys, S. Torquato, and D. P. Bentz, *Phys. Rev. E* **50**, 403 (1994).
- [23] E. J. Garboczi, D. P. Bentz, K. A. Snyder, N. Martys, P. E. Stutzmann, and C. Ferraris, *Modeling and Measuring the Structure and Properties of Cement Based Materials: An Electronic Monograph*, available at: <http://ciks.cbt.nist.gov/>
- [24] L. A. Santaló, *Integral Geometry and Geometric Probability* (Addison-Wesley, Reading, 1976).
- [25] A. Rosenfeld, *Digital Picture Processing* (Academic, New York, 1976).
- [26] C. H. Arns, M. A. Knackstedt, W. V. Pinczewski, and K. R. Mecke, *Phys. Rev. E* **63**, 031112 (2001).
- [27] C. H. Arns, J. Mecke, K. R. Mecke, and D. Stoyan, *Eur. Phys. J. B* **47**, 397 (2005).
- [28] K. R. Mecke, *Int. J. Mod. Phys. B* **12**, 861 (1998).
- [29] K. R. Mecke, in *Statistical Physics and Spatial Statistics: The Art of Analyzing and Modeling Spatial Structures and Pattern Formation*, edited by K. R. Mecke and D. Stoyan, Lecture Notes in Physics Vol. 554 (Springer, Berlin, 2000), pp. 111–184.
- [30] S. T. Hyde, I. S. Barnes, and B. W. Ninham, *Langmuir* **6**, 1055 (1990).
- [31] K. Mecke and A. Seyfried, *Europhys. Lett.* **58**, 28 (2002).
- [32] K. R. Mecke, *J. Stat. Phys.* **102**, 1343 (2001).
- [33] I. Balberg, *Phys. Rev. B* **31**, 4053 (1985).
- [34] E. J. Garboczi, K. A. Snyder, J. F. Douglas, and M. F. Thorpe, *Phys. Rev. E* **52**, 819 (1995).
- [35] D. Stauffer and A. Aharony, *Introduction to Percolation Theory*, 2nd ed. (Taylor & Francis, London, 1994).
- [36] Discretization effects, which have been noted previously when simulating conductivity on model morphologies with curved interfaces cannot be considered here.
- [37] Z. Hashin, *ASME J. Appl. Mech.* **50**, 481 (1983).
- [38] J. P. Straley, *J. Phys. C* **10**, 3009 (1977).
- [39] A. Heiba, M. Sahimi, L. Scriven, and H. Davis, *SPE Reservoir Eng.* **7**, 123 (1992).
- [40] M. Sahimi, *Rev. Mod. Phys.* **65**, 1393 (1993).
- [41] R. B. Stinchcombe, *J. Phys. C* **7**, 179 (1974).
- [42] E. J. Garboczi and A. R. Day, *J. Mech. Phys. Solids* **43**, 1349 (1995).
- [43] C. H. Arns, M. A. Knackstedt, W. V. Pinczewski, and E. G. Garboczi, *Geophysics* **67**, 1396 (2002).
- [44] The better match for the particulate phase (1:0) may be due to the choice of neighborhoods in the elastic simulation. Equation (1) is defined where the grain phase is 26-connected (next-nearest-neighbor) and the inverse phase six-connected (nearest neighbor). Use of a trilinear finite element mimics a 26-neighborhood more so than the six-neighborhood. The prediction of the particulate phase is superior to that of the inverse phase which is consistently overestimated by the solver.
- [45] S. Bakke and P. E. Øren, *SPE J.* **2**, 136 (1997).
- [46] P. E. Øren, S. Bakke, and O. J. Arntzen, *SPE J.* **3**, 324 (1998).
- [47] C. H. Arns, M. A. Knackstedt, and W. V. Pinczewski, *Geophys. Res. Lett.* **29**, 1202 (2002).
- [48] J.-F. Thovert, F. Yousefian, P. Spanne, C. G. Jacquin, and P. M. Adler, *Phys. Rev. E* **63**, 061307 (2001).
- [49] B. P. Flannery, H. W. Deckman, W. G. Roberge, and K. L. D'Amico, *Science* **237**, 1439 (1987).
- [50] J. H. Dunsmuir, S. R. Ferguson, and K. L. D'Amico, *IOP Conference Series*, 1991 (unpublished), Vol. 121, p. 257.
- [51] P. Spanne, J. F. Thovert, C. J. Jacquin, W. B. Lindquist, K. W. Jones, and P. M. Adler, *Phys. Rev. Lett.* **73**, 2001 (1994).
- [52] W. Oh and W. B. Lindquist, *IEEE Trans. Pattern Anal. Mach. Intell.* **21**, 590 (1999).
- [53] W. B. Lindquist and A. Venkatarangan, *Phys. Chem. Earth* **25**, 593 (1999).
- [54] W. B. Lindquist, A. Venkatarangan, J. Dunsmuir, and T. F. Wong, *J. Geophys. Res.* **105**, 21509 (2000).
- [55] C. H. Arns, M. A. Knackstedt, W. V. Pinczewski, and W. B. Lindquist, *Geophys. Res. Lett.* **28**, 3361 (2001).
- [56] I. N. Bronstein and K. A. Semendjajew, *Taschenbuch der Mathematik*, 23rd ed. (Harri Deutsch, Leipzig, 1987).
- [57] T. Saito and J.-I. Toriwaki, *Pattern Recogn.* **27**, 1551 (1994).